An Improved Wave-Vector Frequency-Domain Method for Nonlinear Wave Modeling

Yun Jing, Molei Tao, and Jonathan Cannata

Abstract—In this paper, a recently developed wave-vector frequency-domain method for nonlinear wave modeling is improved and verified by numerical simulations and underwater experiments. Higher order numeric schemes are proposed that significantly increase the modeling accuracy, thereby allowing for a larger step size and shorter computation time. The improved algorithms replace the left-point Riemann sum in the original algorithm by the trapezoidal or Simpson's integration. Plane waves and a phased array were first studied to numerically validate the model. It is shown that the left-point Riemann sum, trapezoidal, and Simpson's integration have first-, second-, and third-order global accuracy, respectively. A highly focused therapeutic transducer was then used for experimental verifications. Short high-intensity pulses were generated. 2-D scans were conducted at a prefocal plane, which were later used as the input to the numerical model to predict the acoustic field at other planes. Good agreement is observed between simulations and experiments.

I. Introduction

ACCURATE and efficient numerical simulations for non-linear/shock wave propagation are critical for understanding many interesting nonlinear acoustic behaviors and could assist the design of therapeutic and imaging ultrasound arrays. Although the Khokhlov–Zabolotskaya–Kuznetsov (KZK) equation [1] has been used for decades for nonlinear wave simulations [2]–[5], new methods have been emerging that are based on the Westervelt equation [6]–[15], which is more accurate, especially in the near field and for highly focused transducers [16]. The Westervelt equation also allows one to model nonlinear scattering, whereas the KZK equation does not [17]. Different types of approaches have been proposed for solving the Westervelt equation. For example, the Westervelt equation can be decomposed into three equations, representing the diffraction, absorption, and nonlinearity [10], [11], [14]. The equation for diffraction can be solved by the angular spectrum approach, and the equation for nonlinearity can be solved either in the frequency domain [4], [18] or time domain [14]. In the time domain, typically the Godunov-type scheme is used if shock waves are present. It is a conservative numerical scheme for solving partial differential equations [19]. The total solution is acquired

by a splitting scheme [10], [20], [21]. These approaches typically assume that the nonlinearity builds up mainly in the direction normal to the transducer surface, and thus have been considered less accurate for highly focused transducers and steering beams [6], [13]. The Westervelt equation can be also solved entirely in the time domain by using the finite-difference time-domain (FDTD) method [22] or k-space method [8], [12]. These methods require more computational resources (even though the k-space method is typically more computationally efficient than the FDTD method), but are typically preferred if the medium under study is heterogeneous. This is because the medium properties (speed, density, and absorption) can be functions of the position, which is generally not possible in angular spectrum methods. Other approaches include an iterative scheme for solving the Westervelt equation [13], in which the nonlinearity and absorption are modeled as contrast source terms. This approach needs the complete time history of the acoustic field (a 4-D matrix) to be stored, which could potentially be a limitation in terms of memory requirement when large-scale problems are to be modeled.

This paper is a follow-up to a recently proposed wave-vector frequency-domain (WVFD) approach [6], [9], [23], which has been proven valid for both weakly nonlinear and acoustic shock waves through numerical simulations. This approach is devised for homogenous media with the potential to be extended to layered structures. It accounts for nonlinearity in arbitrary direction and interaction of all waves propagating in every direction, therefore is expected to be accurate, particularly for highly focused transducers. Because this approach operates in the frequency domain, dispersion and frequency-dependent absorption can be naturally taken into account. In addition, this model can be conveniently used for implementing backward wave propagation, to examine the pressure distribution on the transducer surface or the pressure field on a plane close to the source [6], [23]. In this paper, two modified stepping algorithms in the z-axis are proposed which progressively improve the accuracy of the original WVFD. Although the original algorithm is based on the left-point Riemann sum, the two new algorithms are based on the trapezoidal and Simpson's integrations. Systematic comparisons are carried out between the three algorithms against benchmark solutions. Finally, underwater field measurements using a therapeutic transducer are conducted to further validate the model.

In Section II, the two new stepping algorithms for the WVFD model are formulated, based on the Westervelt equation. Section III discusses comparison between the

original and present algorithms for their accuracies and time costs. The accuracy is determined by comparing different approaches with benchmark solutions for plane waves and a phased array problem. Experimental results using the focused transducer are also shown in this section. Section IV concludes the paper.

II. Theory

We begin with the time-domain Westervelt equation [7], [16]

$$
\nabla^2 p(\mathbf{r}, t) - \frac{1}{c_0^2} \frac{\partial^2}{\partial t^2} p(\mathbf{r}, t) + \frac{\delta}{c_0^4} \frac{\partial^3}{\partial t^3} p(\mathbf{r}, t)
$$
$$
+ \frac{\beta}{\rho c_0^4} \frac{\partial^2}{\partial t^2} p^2(\mathbf{r}, t) = 0, \tag{1}
$$

where p is the sound pressure, c_0 is the speed of sound, δ is the diffusivity, β is the nonlinearity coefficient, and ρ_0 is the density. The last four parameters define the medium properties.

Fourier transformation of the x, y, and t dimensions yields a wave-vector frequency-domain equation:

$$
\frac{\partial^2}{\partial z^2} P(k_x, k_y, z, \omega) + K^2 P(k_x, k_y, z, \omega) - \frac{\beta \omega^2}{\rho_0 c_0^4} P(k_x, k_y, z, \omega)
$$
$$
\otimes P(k_x, k_y, z, \omega) = 0, \tag{2}
$$

where $P(k_x, k_y, z, \omega)$ is the Fourier transform of $p(x, y, z, t)$, and

$$
K^2 = \frac{\omega^2}{c_0^2} - k_x^2 - k_y^2 - i \frac{\delta \omega^3}{c_0^4}, \tag{3}
$$

where ω is the angular frequency, k_x and k_y are the wave numbers, and $\otimes$ represents the convolution in terms of k_x, k_y, and ω.

The solution to (2) is shown to be an integral equation [6], [15],

$$
P(k_x, k_y, z, \omega) = P(k_x, k_y, 0, \omega) e^{iKz}
$$
$$
+ \frac{M}{2iK} e^{iKz} \int_0^z e^{-iKz'} F(P(z')) \mathrm{d}z', \tag{4}
$$

where

$$
F(P(z')) = P(k_x, k_y, z', \omega) \otimes P(k_x, k_y, z', \omega),
$$
$$
M = \frac{\beta \omega^2}{\rho_0 c_0^4}. \tag{5}
$$

To solve this integral equation, a stepping algorithm along the z-direction can be derived based on the left-point Riemann sums, and is written as

$$
P(z + \Delta z) = P(z) e^{iK\Delta z} + \frac{M e^{iK\Delta z}}{2iK} F(P(z)) \times \Delta z. \tag{6}
$$

By projecting the planar acoustic field at the initial/source plane in the forward direction in increments of Δz, it is possible to predict the acoustic field at any plane parallel to the source plane (x-y plane). This approach has been applied to plane waves and nonlinear acoustic field characterization for phased-array transducers [6]. This scheme based on the left-point Riemann sum is robust for weakly nonlinear wave modeling, but it suffers from low accuracy when moderately nonlinear or acoustic shock waves are to be modeled. In these cases, because a large number of harmonics are modeled (more than 100 harmonics for shock wave modeling), an extremely small step size Δz is necessary for stability and reasonable accuracy, which leads to intolerably long computation time. To this end, a first modified scheme is proposed:

$$
P^0(z + \Delta z) = P(z) e^{iK\Delta z} + \frac{M e^{iK\Delta z}}{2iK} F(P(z)) \times \Delta z,
$$
$$
P^1(z + \Delta z) = P(z) e^{iK\Delta z} + \frac{M e^{iK\Delta z}}{2iK}
$$
$$
\times [F(P(z)) + F(P^0(z + \Delta z)) e^{-iK\Delta z}] \times \frac{\Delta z}{2}, \tag{7}
$$

This numerical scheme is based on a trapezoidal approximation of the integral. To acquire the acoustic field P^1 at $z + \Delta z$, two steps are required. In the first step, an approximate acoustic field P^0 at $z + \Delta z$ is estimated using the left-point Riemann sum, i.e., (6). This essentially provides the right-end point value (with a certain error) for the trapezoidal integration, which is then carried out in the second step. Note that the acoustic field at z [$P(z)$] readily provides the left-end point value. The computation time for this scheme is roughly double that of the original one (left-point Riemann-sum-based scheme), because two steps are needed to project the field by Δz. Nevertheless, as will be shown, the significantly higher accuracy gained from this new scheme compensates for its longer computation time. This new scheme can be further improved. The middle and right-end point values can be estimated by the trapezoidal integration and a final step will be implemented via Simpson's rule for integration. Such a scheme can be written as (8), see next page.

The inverse Fourier transform of P^2 provides the final solution, i.e., the pressure at z. For the same Δz, this scheme is roughly 2.5 times more time consuming than the one based on the trapezoidal integration (therefore 5 times more time consuming than the left-point Riemann-sum-based scheme), because it involves five separate steps rather than two steps. However, an improvement in accuracy is also expected. In fact, if we could use the exact Simpson approximation of the Riemann sum, the method will have fourth-order global accuracy, because it is well known that Simpson quadrature has fifth-order local ac-

$$P^0\left(z + \frac{\Delta z}{2}\right) = P(z)e^{iK(\Delta z/2)} + \frac{Me^{iK(\Delta z/2)}}{2iK} F(P(z)) \times \frac{\Delta z}{2},$$

$$P^1\left(z + \frac{\Delta z}{2}\right) = P(z)e^{iK(\Delta z/2)} + \frac{Me^{iK(\Delta z/2)}}{2iK}\left[F(P(z)) + F\left(P^0\left(z + \frac{\Delta z}{2}\right)\right)e^{-iK(\Delta z/2)}\right] \times \frac{\Delta z}{4},$$

$$P^0(z + \Delta z) = P^1\left(z + \frac{\Delta z}{2}\right)e^{iK(\Delta z/2)} + \frac{Me^{iK(\Delta z/2)}}{2iK} F\left(P^1\left(z + \frac{\Delta z}{2}\right)\right) \times \frac{\Delta z}{2}, \tag{8}$$

$$P^1(z + \Delta z) = P^1\left(z + \frac{\Delta z}{2}\right)e^{iK(\Delta z/2)} + \frac{Me^{iK(\Delta z/2)}}{2iK}\left[F\left(P^1\left(z + \frac{\Delta z}{2}\right)\right) + F(P^0(z + \Delta z))e^{-iK(\Delta z/2)}\right] \times \frac{\Delta z}{4},$$

$$P^2(z + \Delta z) = P(z)e^{iK\Delta z} + \frac{Me^{iK\Delta z}}{2iK}\left[F(P(z)) + 4 \times F\left(P^1\left(z + \frac{\Delta z}{2}\right)\right)e^{-iK(\Delta z/2)} + F(P^1(z + \Delta z))e^{-iK\Delta z}\right] \times \frac{\Delta z}{6}.$$

curacy. However, because we do not have the exact right point value, we use a numerical approximation here. We show in the Appendix that the method based on (8) in fact has fourth-order local accuracy, and therefore third-order global accuracy. (It is well known in numerical analysis that global error is one order less than local error, given stability [24].)

III. NUMERICAL STUDIES

A. Plane Waves

Plane waves were first tested to determine the accuracy of the three algorithms by varying the step size Δz. The L2 norm errors were calculated by comparing the numerical results to benchmark solutions. The L2 norm error is defined as

$$\text{error} = \frac{\| p_{\text{num}}(t) - p_{\text{exact}}(t) \|}{\| p_{\text{exact}}(t) \|}, \tag{9}$$

where $\| p(t) \|$ is the least-square norm, p_{num} is the numerical result, and p_{exact} is the benchmark solution.

Initially, the Fubini solution was used as the benchmark solution. However, it was found that for both schemes based on the trapezoidal integration and Simpson's integration, the L2 norm errors quickly dropped to a small quantity and converged, when reducing the step size Δz. This may have occurred because there are other types of errors involved that are independent of the step size, e.g., Fourier transform and convolution. For this reason, numerical solutions with extremely fine step sizes were instead used as the benchmark solutions to examine the error. A sinusoidal burst of ten circles was used as the excitation signal. The frequency was 5 MHz, the initial pressure amplitude was 5 MPa. For the medium, the nonlinearity coefficient was 3.5 and the speed of sound was 1500 m/s. One set of simulations was implemented in which relatively strong nonlinearity was involved. The propagation distance was 0.8 σ (σ is the shock forma-

tion distance). The diffusivity was 5×10^{-5} m^{2}s^{-1}. The second harmonic was 9.5 dB lower than the fundamental frequency. In the simulation, 40 harmonics were considered in the simulation (this was found to be sufficient to minimize the Gibbs effect), and the step size Δz varied with regard to the wavelength (or σ) to generate different results for comparison with the benchmark solution. The benchmark solutions were calculated using a step size of $\lambda/512$, and were based on the most accurate Simpson's integration. Results of the simulations are shown in Table I. A comparison between different approaches is also shown in Fig. 1. Results are shown in both time- and frequency-domain. This comparison only includes the results at $\Delta z = 4\lambda$. Fig. 1(a) shows the results from 35 to 55 MHz. Lower frequencies are not shown here because the difference is not significant. There is no visual difference between the Simpson's integration and the benchmark solution. Small differences (a few decibels) are observed between the trapezoidal integration and the benchmark solution. The left-point Riemann sum significantly underestimates the results and provides the poorest result.

At this point, we have several comments:

1) The left-point Riemann sum error is proportional to the step size, so that as the step size is reduced by half, the error is also approximately reduced by half. Therefore, as expected, the left-point Riemann sum has first-order accuracy [25]. The trapezoidal integration error is proportional to the step size square, i.e., as the step size is reduced by half, the error is reduced to a quarter of its previous magnitude. Therefore, this new scheme has second-order accuracy. The Simpson's integration error is proportional to the step size cubic, and therefore has third-order accuracy and is more accurate than the previous two schemes.

2) The Simpson's integration is shown here to be at least an order of magnitude more accurate than the trapezoidal integration and two orders of magnitude more accurate than the Riemann sum method, provided that the step size is equal or less than 0.2σ.

TABLE I. L2 Norm Errors at the Distance of 0.8σ.

Step size (Δz)	Riemann sum error	Trapezoidal sum error	Simpson's integration error
4λ (0.2σ)	0.066	0.0097	0.00065
2λ (0.1σ)	0.033	0.0025	0.000087
1λ (0.05σ)	0.016	0.00063	0.000011
$1/2\lambda$ (0.025σ)	0.0078	0.00016	0.0000014
$1/4\lambda$ (0.0125σ)	0.0039	0.00004	0.00000019

A step size of $\lambda/512$ and the Simpson's integration were used to generate the benchmark solution.

The Simpson's integration is expected to be progressively more accurate as the step size decreases. This is particularly useful for acoustic shock wave modeling, because the step size will be much smaller than σ. For example, in the last row of Table I, the errors produced by the trapezoidal integration and left-point Riemann sum are 153 and 20 526 times larger than the error produced by Simpson's integration.

3) When considering the same computation time, the Simpson's integration is still significantly advantageous. For a step size of $1/2\lambda$, the Simpson's integration error is 0.0000014. For the same computation time, trapezoidal integration allows a step size of around $0.5/2.5 = 0.2\lambda$ because it is 2.5 times faster, as shown in Section II. The estimated error is $0.00011/2.5^2 = 0.000018$ (here, we take 2 as the order of the accuracy for estimation; 0.00011 is the error at the step size of $1/2\lambda$), which is more than 12 times larger than the Simpson's integration error. Similarly, for the same computation time, the estimated error using the left-point Riemann sum is $0.0078/5 = 0.0016$ (0.0078 is the error at a step size of $1/2\lambda$ and the left-point Riemann sum is five times faster than the Simpson's integration), which is more than 1000 times larger than the Simpson's integration error.

B. Phased Arrays

To further validate the proposed new algorithms, 3-D simulations were also carried out. A 2-D circular phased array was simulated; the simulated medium was human muscle. For simplification, each grid point was assumed to be an element whose phase was varied so that the focal distance was 40 mm. The delay time used to create the focus was calculated by $(d - d_0)/c_0$, where d is the distance from a point on the transducer to the focus and d_0 is the distance from the center of the transducer to the focus. The diameter of the phased array was 20 mm. The size of the x-y plane for the computational domain was 54.2×54.2 mm. The excitation signal was a 6-cycle burst with a center frequency at 1 MHz. The spatial resolution (dx and dy) was $\lambda/4$, where λ is the wavelength in the muscle. The pressure on the transducer surface was 1.35 MPa. (For reference, the shock formation distance for a plane wave at this amplitude is 120 mm; the actual shock formation distance is expected to be smaller because it is a focused beam.) For the simulated human muscle, the sound speed was 1549.9 m/s, the density was 1060 kg/m^3, the nonlinear parameter β was 3.9, and the attenuation $\alpha(f) = a \times f^b$, where a was 0.52 dB/cm and b was 1.1 [6]. The dispersion follows the Kramers–Kronig relations [26]. Up to 40 harmonics were considered in the simulation. A bench-
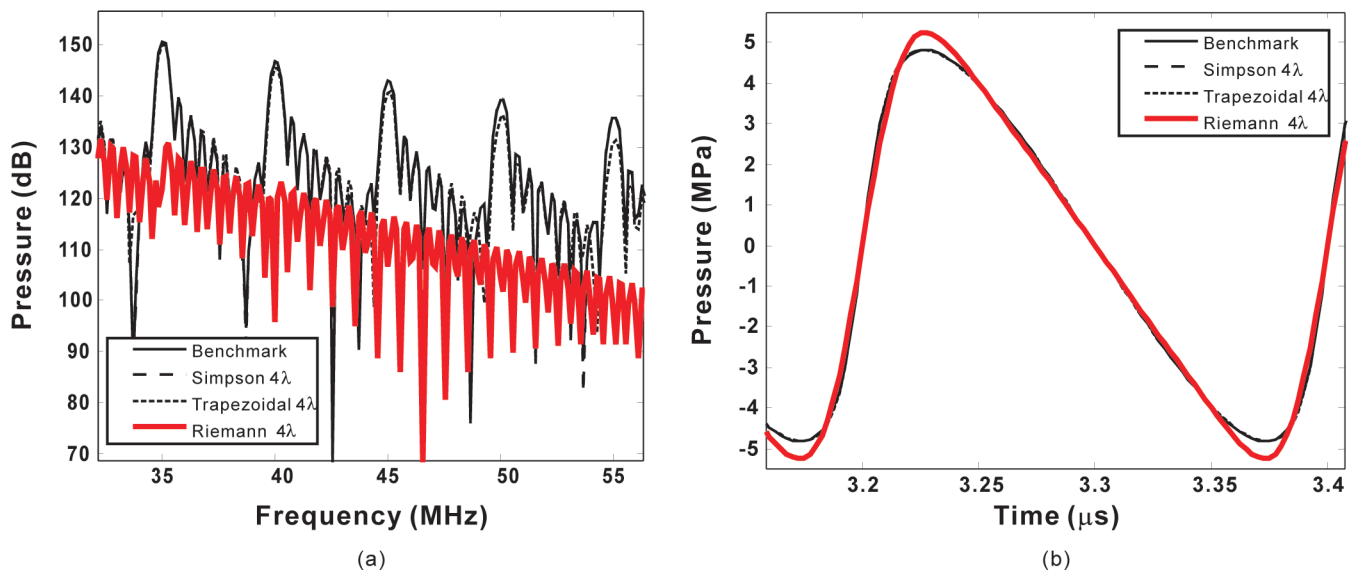

Fig. 1. Comparison between different algorithms for a plane wave in (a) the frequency domain and (b) the time domain. Results with $\Delta z = 4\lambda$ are shown.
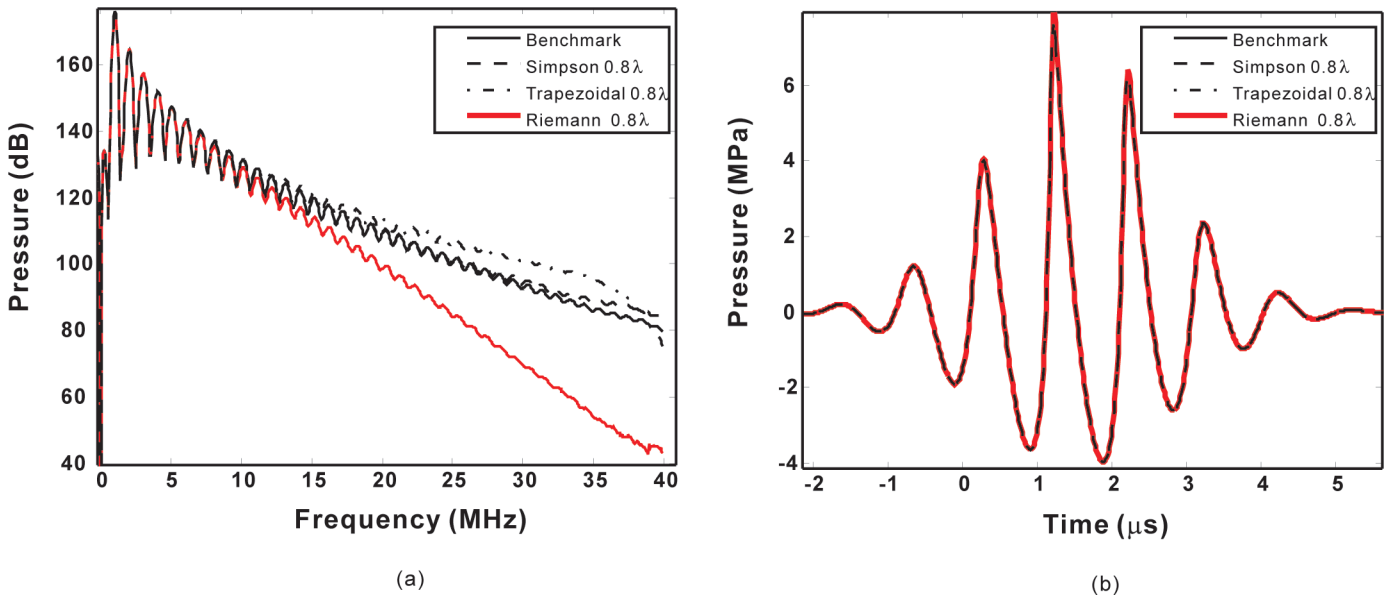
Fig. 2. Comparison between different algorithms for computing the sound field from a phased array in (a) the frequency domain and (b) the time domain. Results with $\Delta z = 0.8\lambda$ are shown here.

mark solution was first generated by using the Simpson's integration with a step size $\Delta z = \lambda/160$. Δz was then varied for different algorithms to evaluate their effectiveness.

Fig. 2 shows the pressure at the focal point in both time and frequency domains, with a same step size $\Delta z = 0.8\lambda$ for the three algorithms. Although the difference is not appreciable in the time domain, the frequency-domain plot shows that the high-frequency harmonics deviate significantly between different algorithms. The Simpson's integration method agrees closely with the benchmark solution. The trapezoidal integration method overestimates the harmonics, and the left-point Riemann sum underestimates the harmonics with the largest error. To evaluate the computational efficiency of the three algorithms, the step size was varied so that the least-square errors of different approaches are approximately the same. To achieve a reasonably small L2 norm error, which is 1.5×10^{-4} as randomly chosen in this study, the Simpson's integration method requires a step size of 0.8λ with a computation time of 423 s, the trapezoidal integration method requires a step size of 0.2λ with a computation time of 605 s, and the left-point Riemann sum requires a step size of 0.00625λ with a computation time of 8500 s. This is about 20 times longer than the time taken by the Simpson's integration method. The computations were implemented by Matlab 2011b (The MathWorks Inc., Natick, MA), on a quad-core 3.60-GHz Intel Xeon 5687 CPU (Intel Corp., Santa Clara, CA).

In this specific problem, where the nonlinearity is still moderate (the second harmonic is about 12 dB lower than the fundamental frequency), the Simpson's method is only slightly better than the trapezoidal method, and they are both significantly more efficient and accurate than the original method based on the left-point Riemann sum. It is expected that for ultrasound with a higher intensity, the

Simpson's integration will be even more superior. This is because more harmonics must be considered, which calls for a smaller step size to avoid the Gibbs effect. To numerically compare the results for higher intensity ultrasound (acoustic shock wave cases) against a benchmark solution is difficult, because computing a benchmark solution is extremely time-consuming, considering that the number of harmonics to be taken into account could be a few hundreds or even thousands, and the step size should be extremely small as well. However, because the Simpson's integration is the highest order approach, in theory it will yield the highest accuracy for small Δz.

IV. EXPERIMENTS

A. Experimental Setup

Experiments were carried out to verify the proposed new algorithm. The experimental setup is illustrated in Fig. 3. We used a custom-made 100-μm-diameter fiber optic hydrophone (HistoSonics Inc., Ann Arbor, MI) for acoustic field mapping [27]. This hydrophone was calibrated with a reference hydrophone (HGL-0085, SN:1258, Onda Corp., Sunnyvale, CA) from 0.25 MHz to 40 MHz following IEC Standard 62127–2: Ultrasonics–Hydrophones–Part 2: Calibration [28] for ultrasonic fields up to 40 MHz. Based on the calibration curve for the reference hydrophone, the uncertainty for the fiber optic hydrophone is 1.5 dB for the range 0.5 to 1 MHz, 1 dB for 1 to 15 MHz, 1.5 dB for 15 to 20 MHz, and 2.2 dB for 20 to 40 MHz.

A spherically focused therapy transducer (Imasonic, Voray-sur-l'Ognon, France) driven by a power amplifier (HistoSonics Inc.) was placed in a distilled water bath degassed to a dissolved oxygen level of 60% or less and
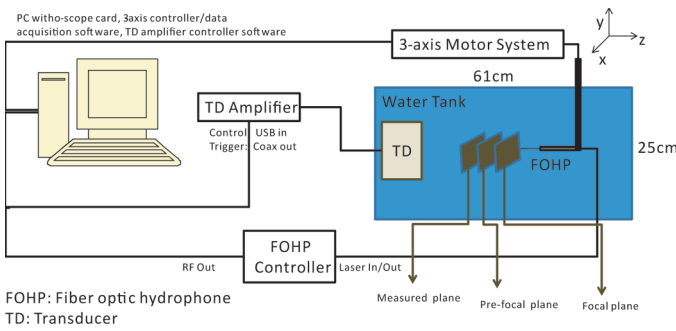
FOHP: Fiber optic hydrophone
TD: Transducer

Fig. 3. Diagram of the experimental setup.

maintained at a temperature of 23.5°C to 24°C. The diameter of the transducer is 13 cm. The focal length of the transducer is 110 mm and the −6 dB axial length for peak positive pressure is 7.7 mm. The excitation signal was a 2-cycle pulse with a center frequency of 700 kHz and a pulse repetition frequency (PRF) of 2 Hz, which was chosen to minimize cavitation on the hydrophone. The transducer focus was located using the fiber optic hydrophone and a 3-axis computer-controlled positioning system (Therus Corp., Redmond, WA). The hydrophone was then repositioned to automatically acquire the data on the 30 mm pre-focal plane with a PCI 5112 acquisition card (National Instruments Corp., Austin, TX).

The scanning area was 60×60 mm with a resolution of 0.5 mm. The average of 100 voltage waveforms obtained by the hydrophone at each point in space was converted to a pressure waveform using the calibration data obtained from the reference hydrophone to produce a 3-D (x, y, and time) pressure data set. The sampling frequency was 80 MHz. Three line scans were obtained, crossing the focal point along the x-, y-, and z-axes to obtain a benchmark for comparison. For the x- and y-axis scans, 8 averages were taken. For the z-axis line scan, unaveraged pressure waveforms were obtained to limit error resulting from occasional cavitation on the hydrophone tip. 2-D scans were not conducted on the focal plane, again because of the potential for cavitation artifacts.

As the result of our measurement, the 30 mm pre-focal plane was the source plane, whose acoustic field was used as the input to the nonlinear wave propagation program. The acoustic fields on other planes can be consequently predicted and compared with the measured one.

B. Results

The numerical simulation was broken down into three steps to reduce computational load. In the first step, the propagation distance was 15 mm, and the data was interpolated to have a spatial resolution of 0.25 mm. The temporal resolution was interpolated to be 6.24 ns (114 harmonics), and Δz was 0.21 mm ($\lambda/10$). In the second step, the propagation distance was 10 mm, the spatial resolution was 0.125 mm, the temporal resolution was 3.12 ns (228 harmonics), and Δz was 0.043 mm ($\lambda/50$). An artifi-

cial diffusivity 7.5×10^{-5} m^{2}s^{-1} was added to reduce the Gibbs noise and maintain the stability of the algorithm. In the last step, the propagation distance was 15 mm, the spatial resolution was 0.125 mm, the temporal resolution was 1.04 ns (687 harmonics), and Δz was 0.024 mm ($\lambda/90$). An artificial diffusivity 17.5×10^{-5} m^{2}s^{-1} was added to reduce the Gibbs noise. The step size Δz is relatively small because the temporal resolution was small, i.e., a large number of harmonics were considered. Nevertheless, an even smaller step size would be required if the previous Riemann-sum-based numerical scheme was used because of its large error, leading to considerably longer computation times. For the medium properties, the speed of sound in the water was assumed to be 1493 m/s, the nonlinearity coefficient was 3.5, and the attenuation coefficient α/f^2 was 25×10^{15} Np/m/Hz^2. Fig. 4(a) shows the pressure at the geometrical focus. Shock fronts can be clearly observed, as demonstrated by Fig. 4(b). Fig. 4(c) shows the comparison in the frequency domain. We obtained good agreement up to the fifth harmonics, with a maximum difference of around 2 dB. Fig. 5(a) illustrates the positive and negative peak pressures along the z-axis from the 30 mm pre-focal to the 10 mm post-focal plane. The line scan started from only around 10 mm pre-focal plane to maximize the signal-to-noise ratio. Figs. 5(b) and 5(c) show the comparison along x- and y-axes crossing the focus. It is noted that experiment results show a lower positive peak pressure around the focal region especially. This is also evident in Fig. 4(b). This could be because the hydrophone was not exactly aligned at the focus [29]. Uncertainty of the hydrophone at high frequencies and a spatial averaging effect of the hydrophone are also expected to add to the inaccuracy of the hydrophone measurements [30].

Other sources of error also exist. For example, according to the Nyquist–Shannon sampling theorem, under perfect conditions (no time jittering and infinite accuracy in amplitude) it is sufficient to use two points per period to define a harmonic signal, which is the case for our measurement. However, a good practice requires using a factor of 5 to mitigate the imperfect conditions. Furthermore, the signal-to-noise ratio degrades quickly with the order of the harmonics and the distance to the center, and this makes accurate measurements extremely challenging. Nevertheless, simulation results and experimental data are in overall good agreement.

V. Conclusions

A wave-vector frequency-domain nonlinear wave propagation model was studied in this paper. Compared with a previous study, improved numerical schemes which utilize the trapezoidal and Simpson's integrations were proposed and both were shown numerically to yield significantly higher accuracy than the original left-point Riemann-sum-based scheme. We both numerically and mathematically showed that the trapezoidal and Simpson's integrations
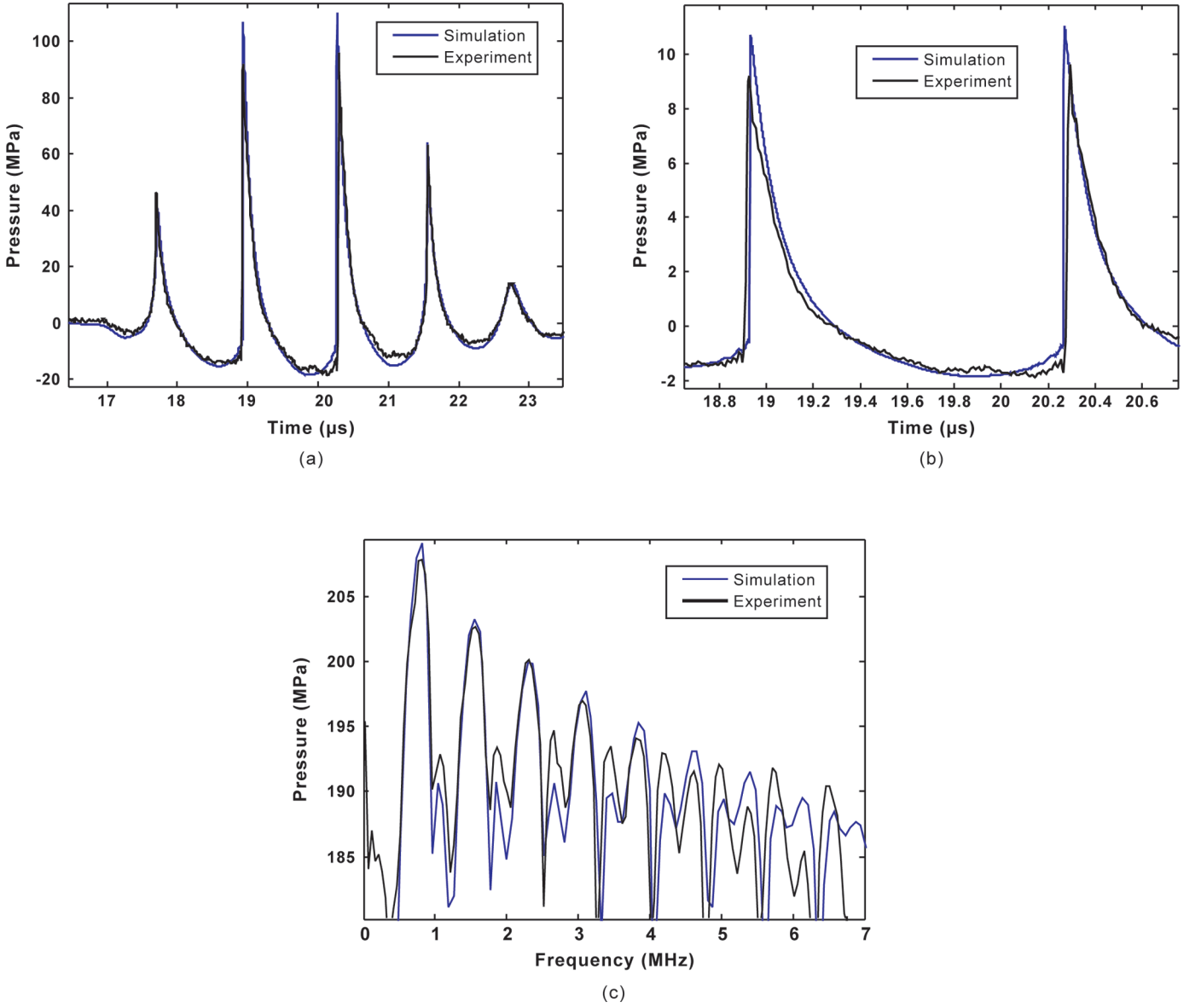
Fig. 4. (a) Simulated and measured waveform at the center of the focal plane; (b) depicts the shock fronts in (a). (c) Results in the frequency domain.

have second-order and third-order global accuracy, respectively. Experimental studies with a therapeutic transducer were carried out which successfully validated the numerical model. Good agreement was found on both pre-focal plane and focal plane. In the future, the model will be extended to allow for the incorporation of layered structures which better represent human bodies.

VI. APPENDIX

In this appendix, we prove that the trapezoidal integration-based algorithm has third-order local accuracy (therefore second-order global accuracy provided stability), and the Simpson's integration-based algorithm has fourth-order local accuracy (therefore third-order global accuracy provided stability).

By applying differentiation with regard to z on both sides of (4), we have

$$
\begin{aligned}
\frac{\partial P(k_x, k_y, z, \omega)}{\partial z} &= iKP(k_x, k_y, 0, \omega)e^{iKz} \\
&\quad + iK\frac{M}{2iK}e^{iKz}\int_0^z e^{-iKz'}F(P(z'))\mathrm{d}z' \\
&\quad + \frac{M}{2iK}F(P(z)) \\
&= iKP(z) + \frac{M}{2iK}F(P(z)).
\end{aligned}
\tag{10}
$$

This is an ODE in the form of $\dot{x} = Ax + f(x)$ with $x(0) = x_0$. Here, to be consistent with standard notations in ODE dynamical systems [31], x is the discretization of P, z is replaced by t, h is the step size (equivalent to dz), $A =$
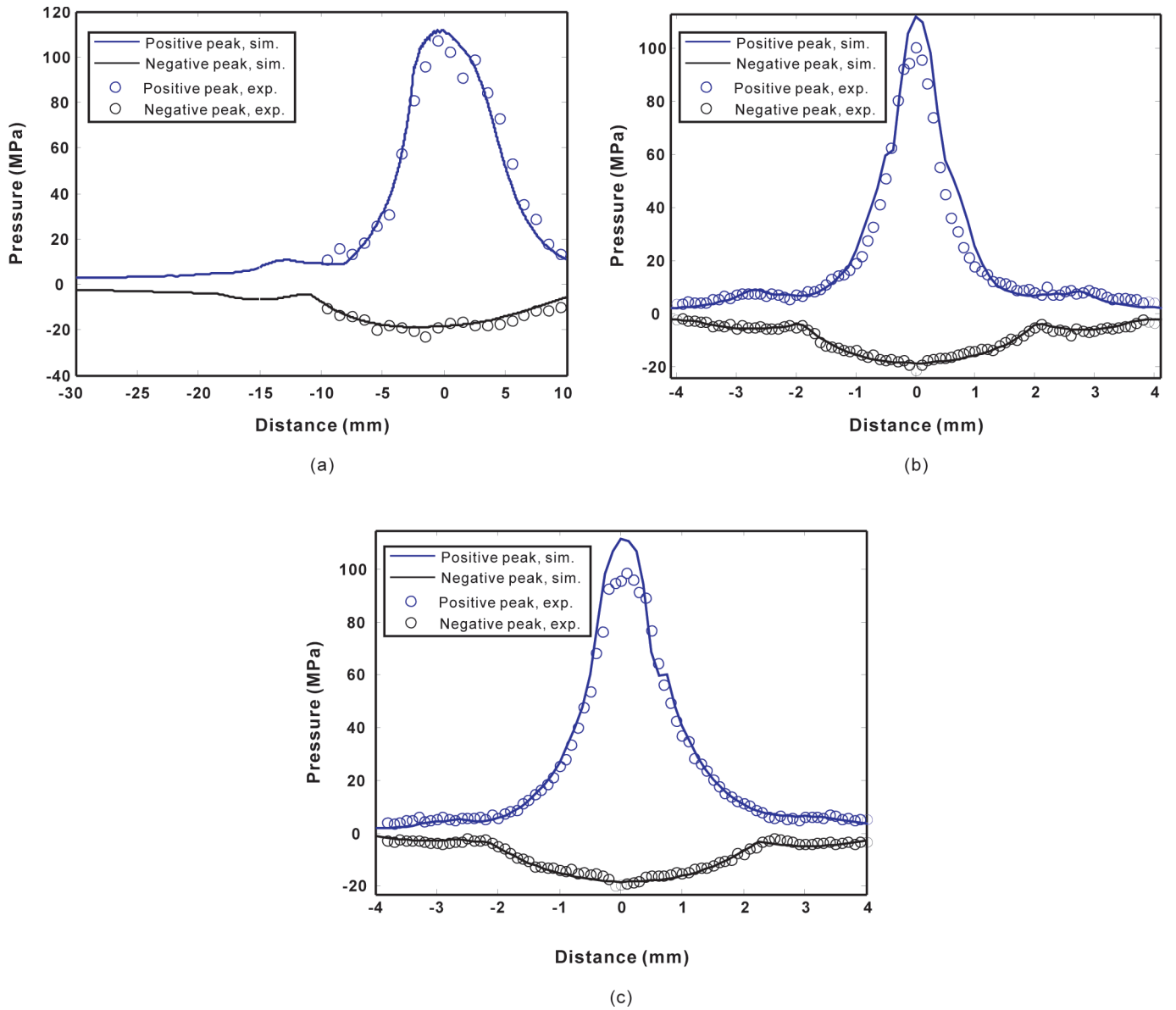
Fig. 5. (a) Simulated and measured positive peak and negative peak pressures along the z-axis. (b) Simulated and measured positive peak and negative peak pressures along the x-axis. (c) Simulated and measured positive peak and negative peak pressures along the y-axis.

iK, $f(x)$ is $(M/(2iK))F(P(z))$, and x_0 is the value of P at the beginning of a step.

Theorem 1 Consider $\dot{x} = Ax + f(x)$ with $x(0) = x_0$. Suppose $f \in \mathcal{C}^4$. Let $G(t) = \exp(At)$. Let

$$\tilde{x}_1 = G(h/2)x_0 + G(h/2)f(x_0)\frac{h}{2} \quad \text{(Riemann sum)} \quad (11)$$

$$\tilde{x}_2 = G(h/2)x_0 + \frac{G(h/2)f(x_0) + f(\tilde{x}_1)}{2}\frac{h}{2} \quad \text{(trapezoidal sum)} \quad (12)$$

$$\hat{x}_1 = G(h/2)\tilde{x}_2 + G(h/2)f(\tilde{x}_2)\frac{h}{2} \quad (13)$$

$$\hat{x}_2 = G(h/2)\tilde{x}_2 + \frac{G(h/2)f(\tilde{x}_2) + f(\hat{x}_1)}{2}\frac{h}{2} \quad (14)$$

$$X = G(h)x_0 + \frac{G(h)f(x_0) + 4G(h/2)f(\tilde{x}_2) + f(\hat{x}_2)}{6}h \quad (15)$$
(final update: Simpson's sum)

Then

$$1) \quad \tilde{x}_1 = x(h/2) + \mathcal{O}(h^2) \quad (16)$$

$$\tilde{x}_2 = x(h/2) + \mathcal{O}(h^3) \quad (17)$$

$$2) \quad \hat{x}_1 = x(h) + \mathcal{O}(h^2) \quad (18)$$

$$\hat{x}_2 = x(h) + \mathcal{O}(h^3) \quad (19)$$

$$3) \quad X = x(h) + \mathcal{O}(h^4), \quad (20)$$

$$\because \ddot{x} = A\dot{x} + f'(x)\dot{x}$$

$$\therefore x(h) = x(0) + h\dot{x}(0) + \frac{h^2}{2}\ddot{x}(0) + \mathcal{O}(h^3)$$

$$= x_0 + h[Ax_0 + f(x_0)] + \frac{h^2}{2}[A + f'(x_0)][Ax_0 + f(x_0)] + \mathcal{O}(h^3)$$

$$\therefore x(h/2) = x_0 + \frac{h}{2}[Ax_0 + f(x_0)] + \frac{h^2}{8}[A + f'(x_0)][Ax_0 + f(x_0)] + \mathcal{O}(h^3)$$

$$\because G(h/2) = I + \frac{h}{2}A + \frac{h^2}{8}A^2 + \mathcal{O}(h^3)$$

$$\therefore \tilde{x}_1 = \left(I + \frac{h}{2}A + \mathcal{O}(h^2)\right)x_0 + [I + \mathcal{O}(h)]f(x_0)\frac{h}{2}$$

$$= x_0 + \frac{h}{2}[Ax_0 + f(x_0)] + \mathcal{O}(h^2)$$

$$= x(h/2) + \mathcal{O}(h^2)$$

$$\tilde{x}_2 = \left[I + \frac{h}{2}A + \frac{h^2}{8}A^2 + \mathcal{O}(h^3)\right]x_0 + \frac{\left[I + \frac{h}{2}A + \mathcal{O}(h^2)\right]f(x_0) + f\left(x_0 + \frac{h}{2}(Ax_0 + f(x_0)) + \mathcal{O}(h^2)\right)}{2}\frac{h}{2}$$

$$= x_0 + \frac{h}{2}Ax_0 + \frac{h^2}{8}A^2x_0 + \frac{f(x_0) + \frac{h}{2}Af(x_0) + f(x_0) + f'(x_0)\frac{h}{2}(Ax_0 + f(x_0)) + \mathcal{O}(h^2))}{2}\frac{h}{2} + \mathcal{O}(h^3)$$

$$= x_0 + \frac{h}{2}(Ax_0 + f(x_0)) + \frac{h^2}{8}(A^2x_0 + Af(x_0) + f'(x_0)(Ax_0 + f(x_0))) + \mathcal{O}(h^3)$$

$$= x(h/2) + \mathcal{O}(h^3)$$

(21)

$$X = G(h)x_0 + \frac{G(h)f(x_0) + 4G(h/2)f(\tilde{x}_2) + f(\hat{x}_2)}{6}h$$

$$= G(h)x_0 + \frac{G(h)f(x_0) + 4G(h/2)f(x(h/2) + \mathcal{O}(h^3)) + f(x(h) + \mathcal{O}(h^3))}{6}h$$

$$= G(h)x_0 + \frac{G(h)f(x_0) + 4G(h/2)f(x(h/2)) + f(x(h)) + \mathcal{O}(h^3)}{6}h$$

$$= G(h)x_0 + \frac{G(h)f(x_0) + 4G(h/2)f(x(h/2)) + f(x(h))}{6}h + \mathcal{O}(h^4)$$

(22)

i.e., the updating rule given by X has a fourth-order local error, which means third-order global error provided stability because of the Lax equivalence theorem [32].

Proof. 1) See (21), above, which proves that the trapezoidal method has third-order local error.

2)

$$\hat{x}_1 = G(h/2)\tilde{x}_2 + G(h/2)f(\tilde{x}_2)\frac{h}{2}$$

$$= G(h/2)(x(h/2) + \mathcal{O}(h^3)) + G(h/2)(f(x(h/2))$$

$$+ \mathcal{O}(h^3))\frac{h}{2}$$

$$= G(h/2)x(h/2) + G(h/2)f(x(h/2)) + \mathcal{O}(h^3).$$

By the same argument in part 1 (the only difference is the starting time; here, the exact solution starts at $x(h/2)$,

spends $h/2$ time, and arrives in $x(h)$; the numerical solution starts at $x(h/2)$, spends $h/2$ time, and arrives at $\hat{x}_1$), we have:

$$G(h/2)x(h/2) + G(h/2)f(x(h/2)) = x(h) + \mathcal{O}(h^2)$$

$$\therefore \hat{x}_1 = x(h) + \mathcal{O}(h^2) + \mathcal{O}(h^3) = x(h) + \mathcal{O}(h^2).$$

Similarly, we have

$$\hat{x}_2 = G(h/2)\tilde{x}_2 + \frac{G(h/2)f(\tilde{x}_2) + f(\hat{x}_1)}{2}\frac{h}{2}$$

$$= G(h/2)x(h/2) + \frac{G(h/2)f(x(h/2)) + f(\hat{x}_1)}{2}\frac{h}{2} + \mathcal{O}(h^3)$$

$$= x(h) + \mathcal{O}(h^3) + \mathcal{O}(h^3) = x(h) + \mathcal{O}(h^3).$$

3) See (22), above. The solution to $\dot{x} = Ax + f(x)$ can be written as

$$x(h) = G(h)x_0 + \int_0^h G(h-s)f(x(s))\mathrm{d}s.$$

The well-known Simpson's rule (quadrature approximation at $s = 0$, $h/2$, h with weights $1/6$, $4/6$, $1/6$) leads to

$$x(h) = G(h)x_0$$
$$+ \frac{G(h)f(x(0)) + 4G(h/2)f(x(h/2)) + G(0)f(x(h))}{6}h$$
$$+ \mathcal{O}(h^5).$$

That is, $x(h) = X + \mathcal{O}(h^4) + \mathcal{O}(h^5) = X + \mathcal{O}(h^4)$. (Note: instead of fourth-order convergence, we only have third-order convergence of the resulting Simpson's-integration-based method. This is due to numerically approximated mid- and right points.)

References

[1] V. Kuznetsov, "Equations of nonlinear acoustics," *Sov. Phys.– Acoust.*, vol. 16, pp. 467–470, 1971.

[2] Y.-S. Lee and M. F. Hamilton, "Time-domain modeling of pulsed finite-amplitude sound beams," *J. Acoust. Soc. Am.*, vol. 97, no. 2, pp. 906–917, 1995.

[3] M. A. Averkiou and R. O. Cleveland, "Modeling of an electrohydraulic lithotripter with the KZK equation," *J. Acoust. Soc. Am.*, vol. 106, no. 1, pp. 102–112, 1999.

[4] V. A. Khokhlova, R. Souchon, J. Tavakkoli, O. A. Sapozhnikov, and D. Cathignol, "Numerical modeling of finite-amplitude sound beams: Shock formation in the near field of a cw plane piston source," *J. Acoust. Soc. Am.*, vol. 110, no. 1, pp. 95–108, 2001.

[5] Y. Jing and R. O. Cleveland "Modeling the propagation of nonlinear three-dimensional acoustic beams in inhomogeneous media," *J. Acoust. Soc. Am.*, vol. 122, no. 3, pp. 1352–1364, 2007.

[6] Y. Jing, M. Tao, and G. Clement, "Evaluation of a wave vector frequency domain method for nonlinear wave propagation," *J. Acoust. Soc. Am.*, vol. 129, no. 1, pp. 32–46, 2011.

[7] Y. Jing, D. Shen, and G. T. Clement, "Verification of the Westervelt equation for focused transducers," *IEEE Trans. Ultrason. Ferroelectr. Freq. Control*, vol. 58, no. 5, pp. 1097–1101, 2011.

[8] Y. Jing, T. Wang, and G. Clement, "A k-space method for moderately nonlinear wave propagation," *IEEE Trans. Ultrason. Ferroelectr. Freq. Control*, vol. 59, no. 8, pp. 1664–1673, 2012.

[9] Y. Jing and G. T. Clement, "On the use of gegenbauer reconstructions for shock wave propagation modeling," *J. Acoust. Soc. Am.*, vol. 130, no. 3, pp. 1115–1124, 2011.

[10] R. J. Zemp, J. Tavakkoli, and R. S. C. Cobbold, "Modeling of nonlinear ultrasound propagation in tissue from array transducers," *J. Acoust. Soc. Am.*, vol. 113, no. 1, pp. 139–152, 2003.

[11] T. Varslot and G. Taraldsen, "Computer simulation of forward wave propagation in soft tissue," *IEEE Trans. Ultrason. Ferroelectr. Freq. Control*, vol. 52, no. 9, pp. 1473–1482, 2005.

[12] B. E. Treeby, J. Jaros, A. P. Pendell, and B. T. Cox, "Modeling nonlinear ultrasound propagation in heterogeneous media with power low absorption using a k-space pseudospectral method," *J. Acoust. Soc. Am.*, vol. 131, no. 6, pp. 4324–4336, 2012.

[13] J. Huijssen and M. D. Verweij, "An iterative method for the computation of nonlinear, wide-angle, pulsed acoustic fields of medical diagnostic transducers," *J. Acoust. Soc. Am.*, vol. 127, no. 1, pp. 33–44, 2010.

[14] P. V. Yuldashev and V. A. Khokhlova, "Simulation of three-dimensional nonlinear fields of ultrasound therapeutic arrays," *Acoust. Phys.*, vol. 57, no. 3, pp. 334–343, 2011.

[15] F. Prieur, T. F. Johansen, S. Holm, and H. Torp, "Fast simulation of second harmonic ultrasound field using a quasi-linear method," *J. Acoust. Soc. Am.*, vol. 131, no. 6, pp. 4365–4375, 2012.

[16] M. F. Hamilton and D. T. Blackstock, *Nonlinear Acoustics*. San Diego, CA: Academic, 1998, pp. 42–56.

[17] G. T. Silva and A. Bandeira, "Difference-frequency generation in nonlinear scattering of acoustic waves by a rigid sphere," *Ultrasonics*, vol. 53, no. 2, pp. 470–478, 2013.

[18] F. P. Curra, P. D. Mourad, V. A. Khokhlova, R. O. Cleveland, and L. A. Crum, "Numerical simulations of heating patterns and tissue temperature response due to high-intensity focused ultrasound," *IEEE Trans. Ultrason. Ferroelectr. Freq. Control*, vol. 47, no. 4, pp. 1077–1089, 2000.

[19] N. S. Bakhvalov, Y. M. Zhileikin, and E. A. Zabolotskaya, *Nonlinear Theory of Sound Beams*. New York, NY: American Institute of Physics, 1987, pp. 1–184.

[20] P. T. Christopher and K. J. Parker, "New approaches to nonlinear diffractive field propagation," *J. Acoust. Soc. Am.*, vol. 90, no. 1, pp. 488–499, 1991.

[21] F. Dagrau, M. Rénier, R. Marchiano, and F. Coulouvrat, "Evaluation of a wave vector frequency domain method for nonlinear wave propagation," *J. Acoust. Soc. Am.*, vol. 130, no. 1, pp. 20–32, 2011.

[22] I. M. Hallaj, R. O. Cleveland, and K. Hynynen, "Simulations of the thermo-acoustic lens effect during focused ultrasound surgery," *J. Acoust. Soc. Am.*, vol. 109, no. 5, pt. 1, pp. 2245–2253, 2001.

[23] Y. Jing, J. Cannata, and T. Wang, "Experimental verification of transient nonlinear acoustical holography," *J. Acoust. Soc. Am.*, vol. 133, no. 5, pp. 2533–2540, 2013.

[24] E. Hairer, S. P. Norsett, and G. Wanner, *Numerical Methods in Scientific Computing*, 2nd ed., Berlin, Germany: Springer, 1993.

[25] G. Dahlquist and A. Bjorck, *Solving Ordinary Differential Equations I*. Philadelphia, PA: SIAM, 2008, pp. 521–538.

[26] K. R. Waters, M. S. Hughes, G. H. Brandenburger, and J. G. Miller, "On a time-domain representation of the Kramers-Kronig dispersion relations," *J. Acoust. Soc. Am.*, vol. 108, no. 2, pp. 556–563, 2000.

[27] J. E. Parsons, C. A. Cain, and J. B. Fowlkes, "Cost-effective assembly of a basic fiber-optic hydrophone for measurement of high-amplitude therapeutic ultrasound fields," *J. Acoust. Soc. Am.*, vol. 119, no. 3, pp. 1432–1440, 2006.

[28] *Ultrasonics–Hydrophones–Part 2: Calibration*, IEC standard IEC 62127-2, 2007.

[29] W. Kreider, P. Yuldashev, O. Sapozhnikov, N. Farr, A. Partanen, M. Bailey, and V. Khokhlova, "Characterization of a multi-element clinical HIFU system using acoustic holography and nonlinear modeling," *IEEE Trans. Ultrason. Ferroelectr. Freq. Control*, vol. 60, no. 8, pp. 1683–1698, 2013.

[30] M. S. Canney, M. R. Bailey, L. A. Crum, V. A. Khokhlova, and O. A. Sapozhnikov, "Acoustic characterization of high intensity focused ultrasound fields: A combined measurement and modeling approach," *J. Acoust. Soc. Am.*, vol. 129, no. 4, pp. 2406–2420, 2008.

[31] L. Perko, *Differential Equations and Dynamical Systems*. New York, NY: Springer-Verlag, 2000, p. 60, ch. 1.10.

[32] G. D. Smith, *Numerical Solution of Partial Differential Equations: Finite Difference Methods*, 3rd ed., Oxford, UK: Oxford University Press, 1985, pp. 67–68.

Yun Jing received a B.S. degree in electronic science and engineering from Nanjing University, China, in 2006 and an M.S. degree from Rensselaer Polytechnic Institute in 2007. He received his Ph.D. degree in architectural acoustics from Rensselaer Polytechnic Institute in 2009. Prior to joining the NC State faculty as an assistant professor at 2011, he was a research fellow at Brigham and Women's Hospital, Harvard Medical School. He specializes in the development of analytic and numerical methods for linear and nonlinear wave propagation in fluids. He is interested in biomedical ultrasound, including ultrasound imaging, therapeutic ultrasound, and ultrasound mediated drug delivery.

Photographs and biographies for **Molei Tao** and **Jonathan Cannata** were unavailable at time of publication.